**ORIGINAL PAPER**

**Sili Liu · Pengfei Li · Kun Hu · Lunyang Zhao**

# Constitutive modeling of brittle–ductile transition in porous rocks: formulation, identification and simulation

**Abstract** This paper presents a two-surface elastoplastic model for brittle–ductile transition behaviors of porous rocks subjected to compressive stresses. Two plastic deformation mechanisms are taken into consideration: plastic shearing at low confining pressure and plastic pore collapse at high confining pressure. For loading in the brittle regime, a unified hardening/softening law is introduced into the Drucker–Prager-type yield criterion to describe the pre-peak hardening and post-peak softening behaviors. A non-associated flow rule is adopted to capture the volumetric compressibility–dilatancy phenomenon. For loading in the ductile regime, a monotonic strain hardening law as a function of hydrostatic stress is proposed and incorporated into the DiMaggio–Sandler-type yield criterion. A non-associated flow rule is used to realistically describe the plastic compaction response caused by non-hydrostatic stress. An analytical solution of stress–strain relations for shear surface is developed in the case of conventional triaxial compression. Based on the bifurcation analysis, the onset of strain localization along cap surface is predicted. Comparisons between numerical simulations and experimental data show that the proposed model is able to capture the main mechanical behaviors of the investigated porous rocks, Adamswiller sandstone and Bentheim sandstone, including strength nonlinearity, strong pressure sensitivity, strain hardening/softening, volumetric compaction/dilation, and brittle–ductile transition.

## 1 Introduction

When subjected to an overall compressive loading, porous rocks may fail by brittle failure or by ductile failure. That is, porous rocks may fault or otherwise deform without loss of compressive strength. Understanding this phenomenon is important for earth sciences and structural geology [1]. To study this phenomenon, a number of laboratory experiments, including mechanical behavior investigation and microstructure analysis of porous rocks, have been carried out under different conditions. Experimental studies have shown that porous

S. Liu · P. Li
College of Civil Engineering, Jiangsu Open University, Nanjing 210036, China
E-mail: liusili300@163.com

P. Li
E-mail: lipengfeihhu@163.com

K. Hu
Faculty of Architecture and Civil Engineering, Huaiyin Institute of Technology, Huaian 223003, China
E-mail: hukunhhu@163.com

L. Zhao (✉)
School of Civil Engineering and Transportation, South China University of Technology, Guangzhou 510641, China
E-mail: nilyang@scut.edu.cn

rocks, such as sandstone, tuff and chalk, undergo a transition in failure mode from localized shear bands to homogeneously distributed deformation throughout the rock with an increase in confining pressure at room temperature [2–6], i.e., low-temperature brittle–ductile transition (BDT). Further, the mechanical behavior of porous rocks is very complex, and characterized by various features: strength nonlinearity, strong pressure sensitivity, strain hardening and softening, dilatancy and friction, compaction and pore collapse, and so forth. However, two basic plastic deformation mechanisms are usually identified. The predominant deformation mechanism associated with macroscopic failure in the brittle regime is microcracking [7–10]. In contrast, plastic deformation in the ductile regime mainly arises from pore collapse and grain crushing [11–15].

For the modeling of these two plastic deformation mechanisms in porous rock, a number of constitutive models have been developed in the general framework of plasticity. For the microcracking mechanism, a pressure sensitive, Mohr–Coulomb-type yield surface and a non-associated flow rule, has been widely employed, for instance, [16–18], among many others. These models can generally describe the pre-peak hardening and post-peak softening behavior, and dilatancy of porous rock in the brittle regime. For the pore collapse mechanism, plastic models with a smooth elliptical yield surface, together with an associated flow rule, have been proposed [19–21]. In particular, two classes of plasticity models are often invoked: critical state models [22] and cap models [23]. These two kind of models have been commonly used for soils, clays, and porous rocks. However, laboratory data and comparison with the critical state models have found it inappropriate to directly apply these models to porous rock, given the certain fundamental differences between soil and rock [24–26]. In order to reasonably describe the nonlinear mechanical responses of porous rock in the ductile regime, many scholars have tried to establish cap models for modeling the strain hardening and volume compaction. For example, Foster et al. [27] formulated a three-invariant, isotropic/kinematic hardening cap plasticity model for porous geomaterials; Tamagnini and Ciantia [28] proposed an extended theory of plasticity with generalized hardening to describe the response of porous geomaterials under both mechanical and environmental processes; Bennett and Borja [29] modified a Drucker–Prager/Cap plasticity model and developed a novel hyper-elastoplastic damage constitutive model for porous rocks; Lv et al. [30] proposed a thermal–mechanical coupling elastoplastic model of freeze–thaw deformation for porous rocks, which couples thermal mechanism and elastoplastic mechanical process. Recent studies have shown that an elliptic cap model is sufficient to describe laboratory data on porous rocks [20,31–33]. For the description of the BDT in porous rocks, various models have been proposed by combining two yield surfaces (a cap surface for plastic pore collapse and a friction surface for plastic shearing, and the two surfaces meet at a vertex) that describe, respectively, the two identified mechanisms of plastic deformation [34–37]. For instance, Lin et al. [38] proposed a Drucker–Prager/Gurson-type plasticity model to account for the pore collapse and plastic shearing mechanisms that govern the mechanical behavior of ductile porous materials; Xie and Shao [39] formulated a poroplastic Mohr–Coulomb/Gurson-type plasticity model to simulate undrained triaxial compression tests of saturated porous geomaterials with variation of interstitial pressure; Jia et al. [40] proposed an elastoplastic model with two yield surfaces (a quadratic Mohr–Coulomb criterion for plastic shearing mechanism and a Gurson-type criterion for pore collapse mechanism) to describe the mechanical behavior of porous concrete under different saturation conditions and high confining pressures. Furthermore, in order to avoid singularity point at the intersection between two surfaces, plastic models with one single yield surface for two mechanisms have been alternatively proposed [41–43].

In spite of great efforts made so far, there are still some shortcomings in existing constitutive models to properly describe the BDT behaviors. For the plastic models with one single yield surface, the stress–strain transition from brittle to ductile behaviors in the brittle regime with the increase in confining pressure are usually ignored. As a consequence, post-peak behavior and residual strength of porous rock are not correctly described. On the other hand, the failure mode transition from dilatant failure in the brittle regime to compactant failure in the ductile regime are also not properly described. For the plastic models with two independent yield surfaces, the evolution of inelastic deformation is generally implicitly assumed to follow an associated flow rule, which is not able to realistically capture the inelastic compaction of porous rock over a broad range of confining pressures.

The purpose of this paper is to develop a new constitutive model for the description of the brittle–ductile transition in porous rocks. The organization of this paper is as follows. In Sect. 2, a two-surface constitutive model is formulated in the framework of plasticity theory. Specific yield criteria, strain hardening/softening laws and plastic potentials are proposed to describe the pre-peak hardening and post-peak softening behaviors in the brittle regime as well as volumetric compressibility–dilatancy transition, and the shear-enhanced compaction in the ductile regime. In Sect. 3, some cases of the proposed model under conventional triaxial compression are presented. In Sect. 4, the predictive capacity of the proposed model is examined by comparing numerical

simulations and experimental data of two typical porous rocks, Adamswiller sandstone (porosity 22.6%) and Bentheim sandstone (porosity 22.8%).

## 2 Presentation of the elastoplastic model for porous rocks

### 2.1 General formulation

The laboratory results suggest that the mechanical behavior of porous rocks can be modeled in terms of elastoplastic model with two deformation mechanisms: plastic shearing mechanism for low confining pressures and plastic pore collapse mechanism for high confining pressures. In this section, we aim at modeling the two evidenced plastic deformation mechanisms by two yield surfaces: a linear surface for the plastic shearing and a cap surface for the plastic pore collapse. With the assumption of isothermal conditions and small strains, it is assumed that the total strain increment $d\boldsymbol{\varepsilon}$ can be decomposed into an elastic and a plastic components, $d\boldsymbol{\varepsilon}^{\mathrm{e}}$ and $d\boldsymbol{\varepsilon}^{\mathrm{p}}$, respectively. The plastic component is then divided into plastic shearing and plastic pore collapse components, $d\boldsymbol{\varepsilon}^{\mathrm{ps}}$ and $d\boldsymbol{\varepsilon}^{\mathrm{pc}}$, respectively:

$$d\boldsymbol{\varepsilon} = d\boldsymbol{\varepsilon}^{\mathrm{e}} + d\boldsymbol{\varepsilon}^{\mathrm{p}}, \quad \text{with} \quad d\boldsymbol{\varepsilon}^{\mathrm{p}} = d\boldsymbol{\varepsilon}^{\mathrm{ps}} + d\boldsymbol{\varepsilon}^{\mathrm{pc}} \tag{1}$$

The elastic strain component $d\boldsymbol{\varepsilon}^{\mathrm{e}}$ is related to the applied stress increment $d\boldsymbol{\sigma}$ through Hooke's law:

$$d\boldsymbol{\varepsilon}^{\mathrm{e}} = \frac{1+\nu}{E} d\boldsymbol{\sigma} - \frac{\nu}{E} \mathrm{tr}\,(d\boldsymbol{\sigma})\,\boldsymbol{\delta} \tag{2}$$

where $E$ and $\nu$ are the Young's modulus and the Poisson's ratio of porous rock, respectively.

According to Eqs. (1) and (2), the general incremental form of stress–strain relation can be written as follows:

$$d\boldsymbol{\sigma} = \mathbb{C} : \left(d\boldsymbol{\varepsilon} - d\boldsymbol{\varepsilon}^{\mathrm{p}}\right) \tag{3}$$

where $\mathbb{C}$ is the elastic stiffness tensor of the porous rock and can be expressed as:

$$\mathbb{C} = 2G\mathbb{K} + 3K\mathbb{J} \tag{4}$$

with $K$ and $G$ being the elastic bulk and shear moduli of the porous rock, respectively. Two isotropic and symmetric fourth order tensors $\mathbb{K}$ and $\mathbb{J}$ are defined by:

$$J_{ijkl} = \frac{1}{3}\delta_{ij}\delta_{kl}, \quad I_{ijkl} = \frac{1}{2}\left(\delta_{ik}\delta_{jl} + \delta_{il}\delta_{ik}\right), \quad \mathbb{K} = \mathbb{I} - \mathbb{J} \tag{5}$$

where $\mathbb{I}$ is the symmetric fourth order unit tensor. $\boldsymbol{\delta}$ denotes the second order unit tensor. In the following, the specific formulations are presented, respectively, for modeling of plastic shearing mechanism and plastic pore collapse mechanism.

### 2.2 Plastic shearing mechanism

For the plastic shearing, plastic deformation is mainly induced by frictional sliding along closed microcracks, and rock failure occurs by localized shearing [44]. Rock mechanics studies have demonstrated that the peak strength in the brittle faulting regime for porous rocks is approximately linearly correlated with confining pressure [4,5,45–47]. For the sake of simplicity, assuming that the shearing yield surface has the same general shape as the failure surface, the following Drucker–Prager-type criterion is used:

$$f_{\mathrm{s}}\left(\boldsymbol{\sigma}, \mu_{\mathrm{s}}\right) = \tau - \mu_{\mathrm{s}}\left(\sigma_{\mathrm{m}} + h\right) \leq 0 \tag{6}$$

with:

$$\sigma_{\mathrm{m}} = \frac{1}{3}\mathrm{tr}\,(\boldsymbol{\sigma}), \quad \tau = \sqrt{\frac{1}{2}\boldsymbol{s}:\boldsymbol{s}} \quad \text{with} \quad \boldsymbol{s} = \boldsymbol{\sigma} - \sigma_{\mathrm{m}}\boldsymbol{\delta} \tag{7}$$

where $h$ represents the hydrostatic tensile strength which is related to material cohesion. The plastic hardening law is described by the evolution of the friction coefficient $\mu_s$ as a function of the plastic equivalent shear strain $\gamma^{ps}$. Laboratory studies on porous rocks have shown that brittle faulting is characterized by pre-peak hardening and post-peak softening behaviors under low confining pressures. The evolution of the function $\mu_s$ should be able to capture the transition from hardening to softening. Inspired by the previous works [48–50], a unified hardening/softening function is here proposed:

$$\mu_s = \mu_0 + \left(\mu_f - \mu_0\right) \frac{N\xi}{N - 1 + \xi^N}, \quad \xi = \gamma^{ps}/\gamma_f^{ps} \tag{8}$$

with:

$$\gamma^{ps} = \int \sqrt{2 de^{ps} : de^{ps}}, \quad de^{ps} = d\varepsilon^{ps} - \frac{1}{3} \mathrm{tr}\left(d\varepsilon^{ps}\right) \delta \tag{9}$$

where $\mu_0$ and $\mu_f$, respectively, characterize the initial and maximum plastic yield thresholds. $\gamma_f^{ps}$ represents the value of plastic equivalent shear strain at the peak stress. The parameter $N$ controls the evolution rate of plastic hardening and softening.

As in most frictional-cohesive geomaterials, there is generally a transition from plastic volumetric compressibility to dilatancy during plastic shearing. Dilatancy is commonly observed as a precursor to brittle faulting in porous rocks [51], which would ultimately lead to failure by strain localization under relatively low confining pressures. Therefore, in order to better describe the dilatancy phenomenon, a non-associated flow rule is needed. To this end, the following plastic potential function is adopted:

$$g_s\left(\boldsymbol{\sigma}, \beta_s\right) = \tau - \beta_s \sigma_m \tag{10}$$

where $\beta_s$ is the dilatancy coefficient, which controls the evolution rate of plastic volumetric strain.

Thus, the plastic strain rate for plastic shearing mechanism is given by:

$$d\boldsymbol{\varepsilon}^{ps} = d\lambda_s \frac{\partial g_s}{\partial \boldsymbol{\sigma}}, \quad \frac{\partial g_s}{\partial \boldsymbol{\sigma}} = -\frac{1}{3} \beta_s \delta + \frac{s}{2\tau} \tag{11}$$

where $d\lambda_s$ is the non-negative plastic multiplier, which can be determined by the plastic consistency condition:

$$df_s = \frac{\partial f_s}{\partial \boldsymbol{\sigma}} : d\boldsymbol{\sigma} + \frac{\partial f_s}{\partial \mu_s} d\mu_s = 0 \tag{12}$$

Accordingly, the plastic multiplier is given as:

$$d\lambda_s = \frac{\frac{\partial f_s}{\partial \boldsymbol{\sigma}} : \mathbb{C} : d\boldsymbol{\varepsilon}}{\frac{\partial f_s}{\partial \boldsymbol{\sigma}} : \mathbb{C} : \frac{\partial g_s}{\partial \boldsymbol{\sigma}} - \frac{\partial f_s}{\partial \mu_s} \frac{\partial \mu_s}{\partial \gamma^{ps}} \frac{\partial g_s}{\partial \tau}} \tag{13}$$

### 2.3 Plastic pore collapse mechanism

In contrast to the plastic shearing mechanism in the brittle field, plastic deformation in the ductile field mainly arise from pore collapse [4,5,11,13,52]. Significant plastic deformation in the form of volume (inelastic compaction) can occur in response to purely hydrostatic loading, due to increasing confining pressure. Under relatively high confining pressures, a shear stress loading would enhance the initiation of inelastic compaction, i.e., the mean stress at the initiation of inelastic compaction is lower than the critical pressure for onset of pore collapse (corresponding to the occurrence of inelastic compaction) under purely hydrostatic loading. At the initiation of inelastic compaction, the mean stress values typically decrease with increasing shear stress, and map out an approximately elliptical cap in the $\tau$ versus $\sigma_m$ plane [5,6,11,15,52–54]. Therefore, for the modeling of plastic pore collapse mechanism in porous rocks, we propose to adopt the DiMaggio–Sandler-type criterion [23] for the formulation of plastic yield function:

$$f_c\left(\boldsymbol{\sigma}, c\right) = \left(\frac{\tau}{c}\right)^2 + \left(\frac{\sigma_m - \sigma_0}{sc}\right)^2 - 1 \le 0 \tag{14}$$

where the parameter $s$ is a constant aspect ratio of the elliptical yield surface, $c$ defines the size of the yield ellipse, and increases with plastic volumetric strain $\varepsilon_v^{pc}$. $sc_0$ and $c_0$ will be used to denote the semi-axes of the initial elliptical cap (for $\varepsilon_v^{pc} = 0$). At high confining pressures, say when the mean stress is close to the plastic pore collapse stress under purely hydrostatic loading, no peak strength can be identified until a very large axial strain is reached. The shear stress–strain curve is continuously increasing with a concave form similar to that in purely hydrostatic loading test. This means that shear-enhanced compaction induced by the applied shear stress under high confining pressures allows the rock to work hardening, thus the development of shear localization is inhibited and compaction localization is formed (which will be discussed in Sect. 3.3). Based on the previous works [39,55–57], the following hardening law is here adopted:

$$c = c_0 \left[ 1 + a \left( \varepsilon_v^{pc} \right)^n \exp \left( b \varepsilon_v^{pc} \right) \right] \tag{15}$$

where $a$, $b$ and $n$ are model parameters that control the plastic hardening rate.

To accurately describe the compressive plastic volumetric deformation in pore collapse process, a non-associated flow rule should be considered. By letting $s'$ differ from $s$ in Eq. (14), the following function is proposed as the plastic potential:

$$g_c \left( \boldsymbol{\sigma}, c \right) = \left( \frac{\tau}{c} \right)^2 + \left( \frac{\sigma_m - \sigma_0}{s'c} \right)^2 \tag{16}$$

where $s'$ is the model parameter of plastic potential, controlling the orientation of the plastic volumetric strain increment.

Thus, the plastic strain rate for plastic pore collapse mechanism writes:

$$d\boldsymbol{\varepsilon}^{pc} = d\lambda_c \frac{\partial g_c}{\partial \boldsymbol{\sigma}}, \quad \frac{\partial g_c}{\partial \boldsymbol{\sigma}} = \frac{2}{3} \frac{(\sigma_m - \sigma_0)}{(s'c)^2} \boldsymbol{\delta} + \frac{s}{c^2} \tag{17}$$

where $d\lambda_c$ is the non-negative plastic multiplier, which can be determined by the plastic consistency condition of $f_c$:

$$df_c = \frac{\partial f_c}{\partial \boldsymbol{\sigma}} : d\boldsymbol{\sigma} + \frac{\partial f_c}{\partial c} dc = 0 \tag{18}$$

Accordingly, the plastic multiplier $d\lambda_c$ is given as:

$$d\lambda_c = \frac{\frac{\partial f_c}{\partial \boldsymbol{\sigma}} : \mathbb{C} : d\boldsymbol{\varepsilon}}{\frac{\partial f_c}{\partial \boldsymbol{\sigma}} : \mathbb{C} : \frac{\partial g_c}{\partial \boldsymbol{\sigma}} - \frac{\partial g_c}{\partial c} \frac{\partial c}{\partial \varepsilon_v^{pc}} \frac{\partial g_c}{\partial \sigma_m}} \tag{19}$$

## 2.4 Interaction between two plastic deformation mechanisms

The existence of two plastic yield surfaces in the proposed model leads to complex law integration. The two plastic deformation mechanisms can be activated either separately or simultaneously. At the intersection of two yield surfaces, the apex regime is a combination of two deformation mechanisms. Therefore, four different possible plastic regimes can be identified.

(1) If $f_s < 0$ and $f_c < 0$, the applied stress state is fully inside the elastic regime, no plastic flow occurs and one gets: $d\lambda_s = 0$ and $d\lambda_c = 0$.

(2) If $f_s = 0$ but $f_c < 0$, only the plastic shearing mechanism is activated. The plastic multiplier $d\lambda_s > 0$ is determined by Eq. (13).

(3) If $f_c = 0$ but $f_s < 0$, only the plastic pore collapse mechanism is activated. The plastic multiplier $d\lambda_c > 0$ is determined by Eq. (19).

(4) If $f_s = 0$ and $f_c = 0$, both the two plastic deformation mechanisms are activated. The plastic multipliers $d\lambda_s > 0$ and $d\lambda_c > 0$ can be determined by the double consistency conditions:

$$df_s = 0, \quad \text{and} \quad df_c = 0 \tag{20}$$

Accordingly, one obtains the system of equations to be solved to determine the plastic multipliers $d\lambda_s$ and $d\lambda_c$

$$\begin{cases} \frac{\partial f_s}{\partial \boldsymbol{\sigma}} : \mathbb{C} : d\boldsymbol{\varepsilon} = \left( \frac{\partial f_s}{\partial \boldsymbol{\sigma}} : \mathbb{C} : \frac{\partial g_s}{\partial \boldsymbol{\sigma}} - \frac{\partial f_s}{\partial \mu_s} \frac{\partial \mu_s}{\partial \gamma^{ps}} \frac{\partial g_s}{\partial \tau} \right) d\lambda_s + \left( \frac{\partial f_s}{\partial \boldsymbol{\sigma}} : \mathbb{C} : \frac{\partial g_c}{\partial \boldsymbol{\sigma}} - \frac{\partial f_s}{\partial \mu_s} \frac{\partial \mu_s}{\partial \gamma^{ps}} \frac{\partial g_c}{\partial \tau} \right) d\lambda_c \\ \frac{\partial f_c}{\partial \boldsymbol{\sigma}} : \mathbb{C} : d\boldsymbol{\varepsilon} = \left( \frac{\partial f_c}{\partial \boldsymbol{\sigma}} : \mathbb{C} : \frac{\partial g_s}{\partial \boldsymbol{\sigma}} - \frac{\partial f_c}{\partial c} \frac{\partial c}{\partial \varepsilon_v^{pc}} \frac{\partial g_s}{\partial \sigma_m} \right) d\lambda_s + \left( \frac{\partial f_c}{\partial \boldsymbol{\sigma}} : \mathbb{C} : \frac{\partial g_c}{\partial \boldsymbol{\sigma}} - \frac{\partial f_c}{\partial c} \frac{\partial c}{\partial \varepsilon_v^{pc}} \frac{\partial g_c}{\partial \sigma_m} \right) d\lambda_c \end{cases} \tag{21}$$

In general case, when both the two plastic mechanisms are activated simultaneously, there is a hardening interaction between the two plastic mechanisms. Shearing induced plastic dilation may affect plastic hardening of pore collapse mechanism. Inversely, pore collapse induced plastic compaction will affect plastic hardening of shearing mechanism. However, in the present work, it seems that Eqs. (8) and (15) can be assumed to be independent of each other. In such a particular case, we can take $\frac{\partial f_s}{\partial \mu_s} \frac{\partial \mu_s}{\partial \gamma^{ps}} \frac{\partial g_c}{\partial \tau} = \frac{\partial f_c}{\partial c} \frac{\partial c}{\partial \varepsilon_v^{pc}} \frac{\partial g_s}{\partial \sigma_m} = 0$, and get a simplified version of Eq. (21). After some mathematical transformations, one gets:

$$\begin{cases} d\lambda_s = \frac{1}{H} \left[ \left( \frac{\partial f_s}{\partial \boldsymbol{\sigma}} : \mathbb{C} : \frac{\partial g_c}{\partial \boldsymbol{\sigma}} \right) \left( \frac{\partial f_c}{\partial \boldsymbol{\sigma}} : \mathbb{C} : d\boldsymbol{\varepsilon} \right) - \left( \frac{\partial f_c}{\partial \boldsymbol{\sigma}} : \mathbb{C} : \frac{\partial g_c}{\partial \boldsymbol{\sigma}} - \frac{\partial f_c}{\partial c} \frac{\partial c}{\partial \varepsilon_v^{pc}} \frac{\partial g_c}{\partial \sigma_m} \right) \left( \frac{\partial f_s}{\partial \boldsymbol{\sigma}} : \mathbb{C} : d\boldsymbol{\varepsilon} \right) \right] \\ d\lambda_c = \frac{1}{H} \left[ \left( \frac{\partial f_c}{\partial \boldsymbol{\sigma}} : \mathbb{C} : \frac{\partial g_s}{\partial \boldsymbol{\sigma}} \right) \left( \frac{\partial f_s}{\partial \boldsymbol{\sigma}} : \mathbb{C} : d\boldsymbol{\varepsilon} \right) - \left( \frac{\partial f_s}{\partial \boldsymbol{\sigma}} : \mathbb{C} : \frac{\partial g_s}{\partial \boldsymbol{\sigma}} - \frac{\partial f_s}{\partial \mu_s} \frac{\partial \mu_s}{\partial \gamma^{ps}} \frac{\partial g_s}{\partial \tau} \right) \left( \frac{\partial f_c}{\partial \boldsymbol{\sigma}} : \mathbb{C} : d\boldsymbol{\varepsilon} \right) \right] \end{cases} \tag{22}$$

with:

$$H = \left( \frac{\partial f_s}{\partial \boldsymbol{\sigma}} : \mathbb{C} : \frac{\partial g_c}{\partial \boldsymbol{\sigma}} \right) \left( \frac{\partial f_c}{\partial \boldsymbol{\sigma}} : \mathbb{C} : \frac{\partial g_s}{\partial \boldsymbol{\sigma}} \right) - \left( \frac{\partial f_s}{\partial \boldsymbol{\sigma}} : \mathbb{C} : \frac{\partial g_s}{\partial \boldsymbol{\sigma}} - \frac{\partial f_s}{\partial \mu_s} \frac{\partial \mu_s}{\partial \gamma^{ps}} \frac{\partial g_s}{\partial \tau} \right) \left( \frac{\partial f_c}{\partial \boldsymbol{\sigma}} : \mathbb{C} : \frac{\partial g_c}{\partial \boldsymbol{\sigma}} - \frac{\partial g_c}{\partial c} \frac{\partial c}{\partial \varepsilon_v^{pc}} \frac{\partial g_c}{\partial \sigma_m} \right) \tag{23}$$

## 3 Some cases for conventional triaxial compression

### 3.1 Analytical stress–strain relations for shear surface

For a conventional triaxial compression test, the stress state is such that $\boldsymbol{\sigma} = [\sigma_1, \sigma_2, \sigma_3]$ with the algebra sequence $\sigma_1 > \sigma_2 = \sigma_3 \geqslant 0$. The corresponding deviatoric part $\boldsymbol{s}$ is given by:

$$\boldsymbol{s} = \frac{1}{3} (\sigma_1 - \sigma_3) [2, -1, -1] \tag{24}$$

According to Eq. (11), the direction of plastic flow rate $\boldsymbol{D} = \frac{\partial g_s}{\partial \boldsymbol{\sigma}}$ in the conventional loading path can be expressed as follows:

$$\boldsymbol{D} = -\frac{1}{3} \beta_s [1, 1, 1] + \left[ \frac{1}{\sqrt{3}}, -\frac{1}{2\sqrt{3}}, -\frac{1}{2\sqrt{3}} \right] \tag{25}$$

As the dilatancy coefficient $\beta_s$ is constant, the direction of plastic flow rate $\boldsymbol{D}$ is also constant. In this way, the current value of plastic strain can be measured by the accumulated value of plastic multiplier such that:

$$\boldsymbol{\varepsilon}^{ps} = \lambda_s \boldsymbol{D} \quad \text{with} \quad \lambda_s = \int d\lambda_s \tag{26}$$

On the other hand, the plastic strain can be decomposed into two parts: the mean part $\frac{1}{3} \varepsilon_v^{ps} \boldsymbol{\delta}$ and the deviatoric part $\boldsymbol{e}^{ps}$

$$\boldsymbol{\varepsilon}^{ps} = \frac{1}{3} \varepsilon_v^{ps} \boldsymbol{\delta} + \boldsymbol{e}^{ps} \tag{27}$$

According to the equivalence between Eqs.(26) and (27), one gets:

$$\varepsilon_v^{ps} = \lambda_s \frac{\partial g_s}{\partial \sigma_m} = -\beta_s \lambda_s, \quad \gamma^{ps} = \lambda_s \frac{\partial g_s}{\partial \tau} = \lambda_s \tag{28}$$

Thanks to the salient features above, the following procedure is proposed to obtain an analytical solution for the stress–strain relations:

(1) Given a plastic equivalent shear strain $\gamma^{\mathrm{ps}}$, calculate $\mu_{\mathrm{s}}$ by using Eq. (8).
(2) Calculate $\sigma_1$ with the prescribed confining pressure $\sigma_3$ and the current value of $\mu_{\mathrm{s}}$ by using Eq. (6)

$$\sigma_1 = \frac{\sqrt{3} + 2\mu_{\mathrm{s}}}{\sqrt{3} - \mu_{\mathrm{s}}} \sigma_3 + \frac{3\mu_{\mathrm{s}} h}{\sqrt{3} - \mu_{\mathrm{s}}} \tag{29}$$

(3) Determine the strain using the relation

$$\boldsymbol{\varepsilon} = \mathbb{S} : (\boldsymbol{\sigma} - \sigma_3 \boldsymbol{\delta}) + \boldsymbol{\varepsilon}^{\mathrm{ps}} \tag{30}$$

where $\mathbb{S} = \mathbb{C}^{-1}$ is the elastic compliance tensor of the porous rock.

The strain components are given by:

$$\begin{aligned}
\varepsilon_1^{\mathrm{s}} &= \frac{1}{E}\sigma_1 - \frac{2\nu}{E}\sigma_3 + \left(\frac{1}{\sqrt{3}} - \frac{1}{3}\beta_{\mathrm{s}}\right)\gamma^{\mathrm{ps}} \\
\varepsilon_2^{\mathrm{s}} &= \varepsilon_3^{\mathrm{s}} = \frac{1-\nu}{E}\sigma_3 - \frac{\nu}{E}\sigma_1 - \left(\frac{1}{2\sqrt{3}} + \frac{1}{3}\beta_{\mathrm{s}}\right)\gamma^{\mathrm{ps}}
\end{aligned} \tag{31}$$

It is noted that the above analytical solution is derived under the assumption of for rate independent. In this circumstance, there is no discrepancy between the analytical and numerical solution for the stress state under shear surface.

## 3.2 Non-associated flow rule and plastic volumetric strain

For plastic shearing mechanism, the friction coefficient $\mu_{\mathrm{s}} = -\left(\partial f_{\mathrm{s}}/\partial\sigma_{\mathrm{m}}\right)/\left(\partial f_{\mathrm{s}}/\partial\tau\right)$ is the local slope of the yield surface in the stress space. Similarly, the dilatancy coefficient $\beta_{\mathrm{s}} = -\left(\partial g_{\mathrm{s}}/\partial\sigma_{\mathrm{m}}\right)/\left(\partial g_{\mathrm{s}}/\partial\tau\right)$ is the local slope of the plastic potential, and it relates the increment of plastic volumetric strain to the increment of plastic equivalent shear strain by the relation $\mathrm{d}\varepsilon_{\mathrm{v}}^{\mathrm{ps}} = -\beta_{\mathrm{s}}\mathrm{d}\gamma^{\mathrm{ps}}$. Here $\beta_{\mathrm{s}}$ is positive, representing dilatancy, as appropriate for porous rocks under low confining pressures.

According to the analytical solution presented above [Eq. (31)], the total volumetric strain $\varepsilon_{\mathrm{v}}^{\mathrm{s}}$ generated by deviatoric stress can be written in the following form:

$$\varepsilon_{\mathrm{v}}^{\mathrm{s}} = \varepsilon_{\mathrm{v}}^{\mathrm{e}} + \varepsilon_{\mathrm{v}}^{\mathrm{ps}} = \frac{(\sigma_1 - \sigma_3)}{E}(1 - 2\nu) - \beta_{\mathrm{s}}\gamma^{\mathrm{ps}} \tag{32}$$

The dilatancy coefficient $\beta_{\mathrm{s}}$ has a significant influence on volumetric compressibility to dilatancy transition (volumetric C/D transition). More precisely, the dilatancy phenomenon is enhanced when the value of $\beta_{\mathrm{s}}$ increases, as shown in Fig. 1.

Following [4], the dilatancy coefficient $\beta_{\mathrm{c}}$ for plastic pore collapse mechanism can be derived from the $\mathrm{d}\varepsilon_{\mathrm{v}}^{\mathrm{pc}}/\mathrm{d}\varepsilon_1^{\mathrm{pc}}$ values evaluated from laboratory data, such that:

$$\beta_{\mathrm{c}} = -\frac{\mathrm{d}\varepsilon_{\mathrm{v}}^{\mathrm{pc}}}{\mathrm{d}\gamma^{\mathrm{pc}}} = -\sqrt{3}\frac{\mathrm{d}\varepsilon_{\mathrm{v}}^{\mathrm{pc}}/\mathrm{d}\varepsilon_1^{\mathrm{pc}}}{\left(3 - \mathrm{d}\varepsilon_{\mathrm{v}}^{\mathrm{pc}}/\mathrm{d}\varepsilon_1^{\mathrm{pc}}\right)} \tag{33}$$

with

$$\mathrm{d}\varepsilon_{\mathrm{v}}^{\mathrm{pc}}/\mathrm{d}\varepsilon_1^{\mathrm{pc}} = \frac{3}{1 + \sqrt{3}\,(s')^2\,[\tau/\,(\sigma_{\mathrm{m}} - \sigma_0)]} \tag{34}$$

Two important consequences can be noted from Eqs. (33) and (34). First, it implies that the volume contracts ($\beta_{\mathrm{c}} < 0$) for mean stress greater than $\sigma_0$. Second, under purely hydrostatic loading ($\tau = 0$), the ratio of increment of plastic volumetric strain to plastic increment of axial strain is $\mathrm{d}\varepsilon_{\mathrm{v}}^{\mathrm{pc}} = 3\mathrm{d}\varepsilon_1^{\mathrm{pc}}$, which of course applies if the behavior is isotropic.

To test the non-associated condition on plastic volumetric strain, we first carry out a sensitivity study of $s'$ involved in Eq. (34). The value of $s'$ varies from 0.70 to 1.70. In Fig. 2, one can see that it mainly influences the evolution rate of plastic deformation. Generally, the plastic volumetric strain will increase as the value of $s'$ decreases.
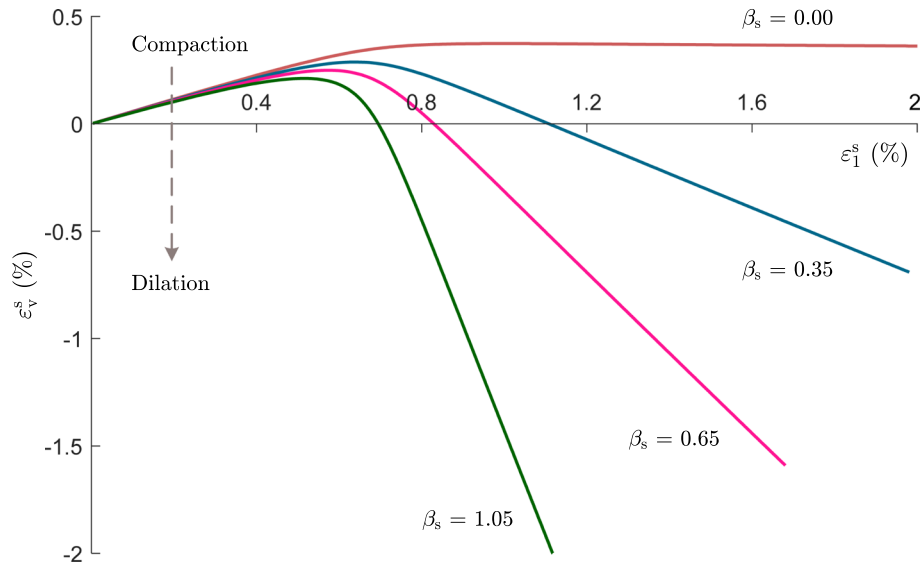
**Fig. 1** Influence of dilatancy coefficient $\beta_s$ on volumetric C/D transition under a uniaxial compression test
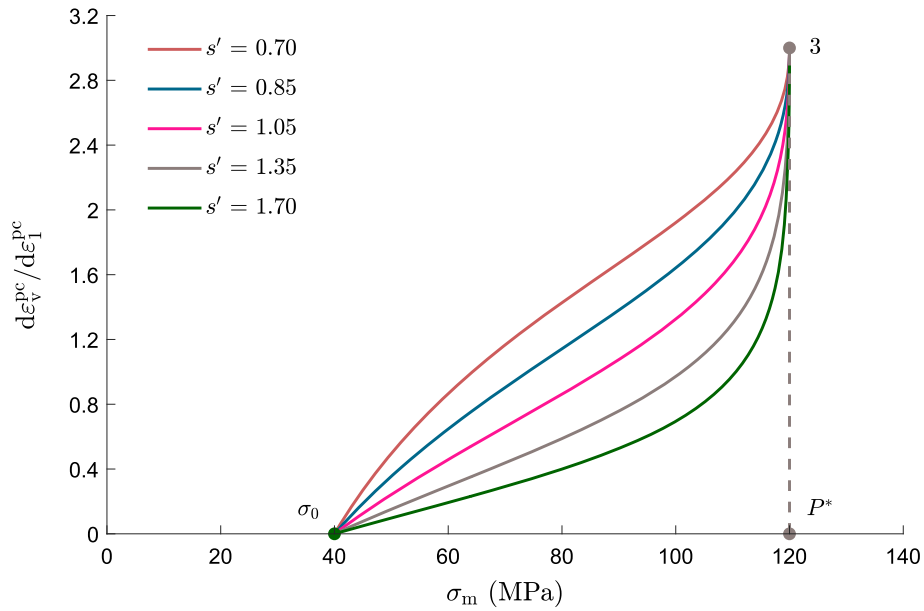


**Fig. 2** Sensitivity analysis of the dilatancy parameter $s'$ ($P^*$ represents the critical stress state for hydrostatic experiment)

### 3.3 Failure mode transition along cap surface

When the stress state is on the cap surface, the failure mode will evolve from shear band to compaction band as the constitutive parameters $\mu_c$ ($\mu_c = -\frac{\partial f_c/\partial \sigma_m}{\partial f_c/\partial \tau} = -\frac{\sigma_m - \sigma_0}{\tau s^2}$) and $\beta_c$ decrease with increasing mean stress. Bifurcation analyses [32,58–60] specify the critical conditions for the incipiency of strain localization, thus providing a theoretical framework for understanding how this transition in failure mode arises from constitutive behavior.

For stress state with $\sigma_m > \sigma_0$, plastic response is characterized by compactant hardening. By using Eq. (15) and taking the derivative of Eq. (14), we can obtain the plastic compaction response caused by hydrostatic loading

$$d\varepsilon_v^{pc} = \frac{d\sigma_m}{k_1} \tag{35}$$

where $k_1 = sac_0 \left(n + b\varepsilon_{\mathrm{v}}^{\mathrm{pc}}\right) \left(\varepsilon_{\mathrm{v}}^{\mathrm{pc}}\right)^{n-1} \exp\left(b\varepsilon_{\mathrm{v}}^{\mathrm{pc}}\right)$ is the plastic bulk hardening modulus.

For non-hydrostatic loading, the plastic volumetric strain response is determined by applying Eqs. (15) and (35) to the derivative of Eq. (14), resulting in

$$\mathrm{d}\varepsilon_{\mathrm{v}}^{\mathrm{pc}} = \left.\frac{\mathrm{d}\sigma_{\mathrm{m}}}{k_2}\right|_{\tau=\mathrm{const}} \quad \text{with} \quad k_2 = \frac{1}{sc}\left[(\sigma_{\mathrm{m}} - \sigma_0) + \frac{\tau}{|\mu_{\mathrm{c}}|}\right]k_1 \tag{36}$$

Equation (36) shows that as the mean stress increases, the plastic volumetric strain response increases from the cap peak $k_2 \to \infty$ to $k_2 = k_1$ at the hydrostatic response. Obviously, by applying $k_1 = 0$ in Eq. (36), we can get the critical value of $k_2 = 0$, and consequently, the slope of the hydrostatic stress versus plastic volumetric strain curve is flat. In this case, a transition in failure mode is predicted to occur if the trade-off between the dilatancy and frictional parameters is such that

$$\mu_{\mathrm{c}} + \beta_{\mathrm{c}} < -\sqrt{3} \tag{37}$$

It should be noted that shear bands are predicted to develop not only for the shear surface, but also for part of the cap surface.

For a conventional triaxial compression test, increase in the axial stress with fixed confining pressure causes $\tau$ to $\sigma_{\mathrm{m}}$ increase in the ratio $\sqrt{3}$. Therefore, the confining pressure that corresponds to the initial cap peak $(\sigma_0, c_0)$ is given by:

$$P^{BDT} = P^* - sc_0 - \frac{c_0}{\sqrt{3}} \tag{38}$$

The condition [Eq. (37)] defines the minimum value of confining pressure for which compaction bands are the only mode of localized deformation that is predicted:

$$P^{CB} = P^* - sc_0 \left[1 - \frac{1 - \left(1/\chi^2 + 1\right)/\left(3s^2\right)}{\sqrt{1 + \left(1/\chi^2 + 1\right)^2/\left(3s^2\right)}}\right] \tag{39}$$

where $\chi = s'/s$ is equal to one if normality is satisfied.

The loading paths for conventional triaxial compression under the two critical confining pressures $P^{BDT}$ and $P^{CB}$ are shown as dashed lines in Fig. 3. At confining pressures lower than $P^{BDT}$, the porous rock will fail by shear band accompanied by strain softening, with dilatancy that initiating in the pre-peak stage. At confining pressures greater than $P^{CB}$, the porous rock will fail by compaction band with monotonic strain hardening. In the transitional regime with $P^{BDT} \leqslant P \leqslant P^{CB}$, the porous rock first experiences strain hardening, the yield cap maintains an elliptical shape and progressively shifts to higher $\sigma_{\mathrm{m}}$ values with the accumulation of plastic volumetric strain; after undergoing certain amount of strain hardening, the maximum shear surface is intersected by the deviatoric loading path, the porous rock then switches from shear-enhanced compaction to dilatancy; after attaining a peak stress, the porous rock encounters strain softening and ultimately fails by shear band [4].

Figure 4 shows the influence of non-normality $\chi$ on the critical confining pressure $P^{CB}$. One can see that non-normality $\chi$ has a significant influence on the critical confining pressure $P^{CB}$. Small change in $\chi$ can cause large change in $P^{CB}$. For example, an increase in $\chi$ of 0.4 could lead to an increase in $P^{CB}$ of as much as 24 MPa. Therefore, in order to achieve a more accurate prediction of the inception of compaction localization, the non-normality condition is needed.

## 4 Model validation

In this section, the performance of the proposed model is validated against laboratory tests obtained on two typical porous rocks, namely, Adamswiller sandstone (porosity 22.6%) and Bentheim sandstone (porosity 22.8%).
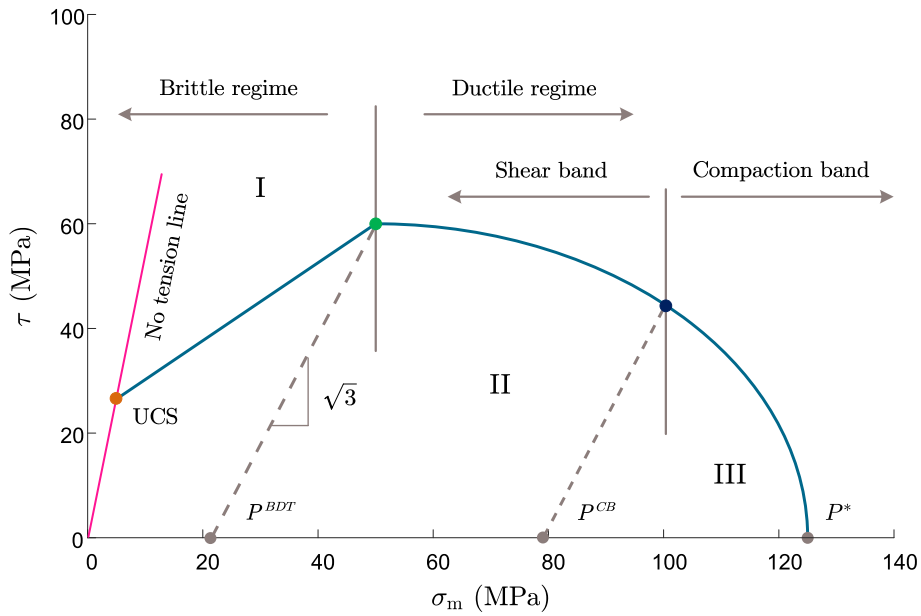
**Fig. 3** Schematic diagram illustrating the brittle–ductile transition and strain localization in the $(\sigma_m, \tau)$ stress space (I - Shear band with pre-peak dilatancy and post-peak softening; II - Shear band with pre-peak hardening and post-peak dilatancy; III - Compaction band with monotonic strain hardening)
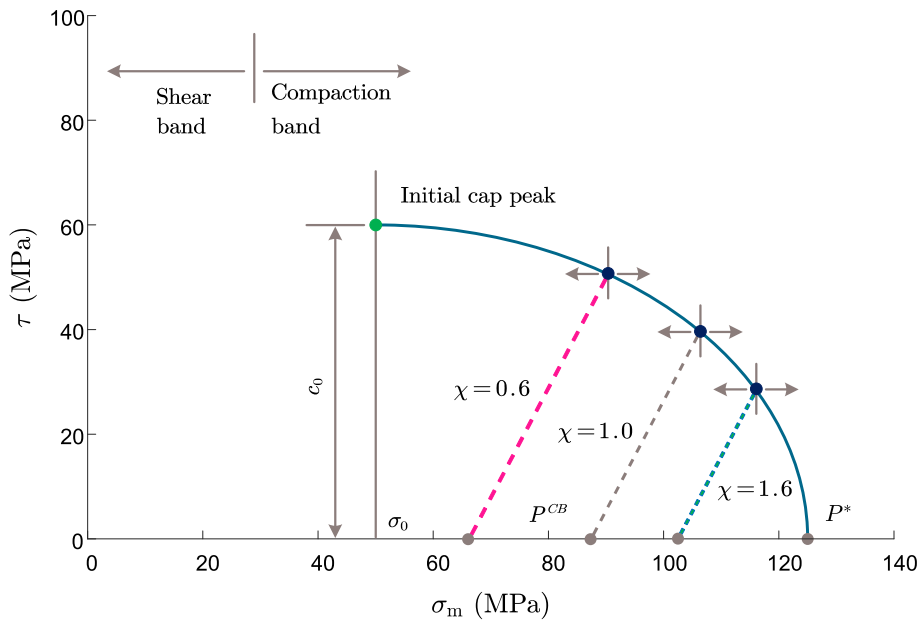


**Fig. 4** Influence of non-normality $\chi$ on critical confining pressure $P^{CB}$

## 4.1 Identification of model parameters

The proposed elastoplastic constitutive model contains 15 parameters: two elastic parameters for the intact rock, six parameters for the plastic shearing mechanism, and seven parameters for the plastic pore collapse mechanism. A minimum of four tests are needed to determine all the parameters. At least two low confining pressure triaxial compression tests are needed to locate the shear surface and to define the shear evolution. A hydrostatic compression test is needed to locate the initial elliptical cap surface and to define the cap evolution, and one additional high confining pressure triaxial compression test is needed to define the elliptical shape of the cap surface.

### 4.1.1 Elastic parameters

The elastic behavior of the rock is characterized by Young's modulus $E$ and Poisson's ratio $\nu$. The two elastic parameters ($E$ and $\nu$) can be directly obtained from the initial linear part of stress–strain curves in uniaxial or triaxial compression tests.

### 4.1.2 Parameters of plastic shearing mechanism

- The plot in the $(\sigma_\mathrm{m}, \tau)$ plane of the initial yield stresses and of the peak stresses provides two straight lines with respective slopes of $\mu_0$ and $\mu_f$. The hydrostatic tensile strength $h$ is given by the intersection of these two straight lines with the mean stress axis.
- For a conventional triaxial compression test, the value of plastic equivalent shear strain at the peak stress $\gamma_f^{\mathrm{ps}}$ can be calculated as:

$$\gamma_f^{\mathrm{ps}} = \frac{2}{\sqrt{3}} \left| \left(\varepsilon_1^{\mathrm{s}} - \varepsilon_3^{\mathrm{s}}\right)_f - \frac{(\sigma_1 - \sigma_3)_f}{E} (1 - \nu) \right| \tag{40}$$

where $(\sigma_1 - \sigma_3)_f$ is the peak stress and $\left(\varepsilon_1^{\mathrm{s}} - \varepsilon_3^{\mathrm{s}}\right)_f$ is the strain difference between axial and lateral directions, corresponding to the peak stress.
- The plot in the $(\sigma_\mathrm{m}, \tau)$ plane of the residual stresses provides a straight line with a slope of $\mu_r$; following Eq. (40), the value of plastic equivalent shear strain $\gamma_r^{\mathrm{ps}}$ at the residual stress is calculated; substituting $\gamma_r^{\mathrm{ps}}$ into Eq. (8), the parameter $N$ can be determined.

The two parameters $N$ and $\gamma_f^{\mathrm{ps}}$ play a role of controlling the evolution rate of strain hardening and softening. Therefore, a sensitivity study of $N$ and $\gamma_f^{\mathrm{ps}}$ is here performed under a uniaxial compression test, as shown in Fig. 5.

In Fig. 5a, one can see that the parameter $N$ has a significant influence on the post-peak stress–strain curve. More precisely, the residual stress increases with the decrease in $N$, the post-peak behavior can be gradually transformed from brittle failure to ductile failure. The influences of $\gamma_f^{\mathrm{ps}}$ on macroscopic stress–strain curves are shown in Fig. 5b. One can see that the post-peak behavior exhibits a transition from brittle failure to ductile failure with the increase in $\gamma_f^{\mathrm{ps}}$. However, unlike the parameter $N$, the axial strain at the peak stress increases with increasing $\gamma_f^{\mathrm{ps}}$, implying that the pre-peak hardening effect increases with the gradual increase in $\gamma_f^{\mathrm{ps}}$. It is worth noting that both the two parameters $N$ and $\gamma_f^{\mathrm{ps}}$ have no effect on the peak stress, they mainly influence the shape of macroscopic stress–strain curve.

- The dilatancy coefficient $\beta_\mathrm{s}$ can be determined from the transition point where the volumetric strain switches from compressibility to dilatancy.
  It is easily to identify the deviatoric stress and volumetric strain (corresponding to the maximum volumetric strain $\varepsilon_{\mathrm{v,max}}^{\mathrm{s}}$) at the volumetric C/D transition point. The combination of Eqs.(40) and (32) allows the determination of the dilatancy coefficient $\beta_\mathrm{s}$.

### 4.1.3 Parameters of plastic pore collapse mechanism

- The maximum shear surface and initial cap surface intersect at the cap peak $(\sigma_0, c_0)$. Therefore, a minimum of two tests are needed to determine the aspect ratio $s$, say $s$ can be fitted from a hydrostatic compression test with one high confining pressure triaxial compression test by drawing the initial yield stresses, as shown in Fig. 6.
- The plastic pore collapse pressure $P^*$ ($P^* = \sigma_0 + sc_0$) can be directly evaluated from the hydrostatic compression test, its value corresponds to the mean stress after which inelastic compaction occurs during this test.
- The parameters $a$, $b$ and $n$ related to the plastic hardening can be identified from a hydrostatic compression test. Specifically, according to Eqs. (14) and (15), under purely hydrostatic compression ($\tau = 0$), one gets:

$$\sigma_\mathrm{m} = \sigma_0 + sc_0 \left[ 1 + a \left(\varepsilon_\mathrm{v}^{\mathrm{pc}}\right)^n \exp\left(b\varepsilon_\mathrm{v}^{\mathrm{pc}}\right) \right] \tag{41}$$

Then, $a$, $b$, and $n$ can be obtained by drawing total volumetric strain versus mean stress with Eq. (41), as illustrated in Fig. 7.
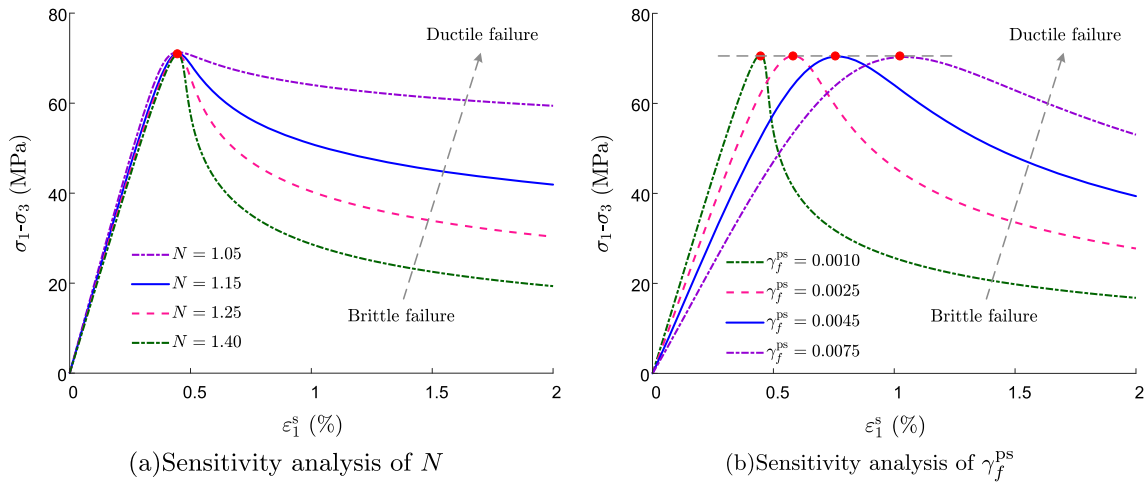
(a)Sensitivity analysis of $N$               (b)Sensitivity analysis of $\gamma_f^{\mathrm{ps}}$

**Fig. 5** Sensitivity analyses of the parameters $N$ and $\gamma_f^{\mathrm{ps}}$ under a uniaxial compression test
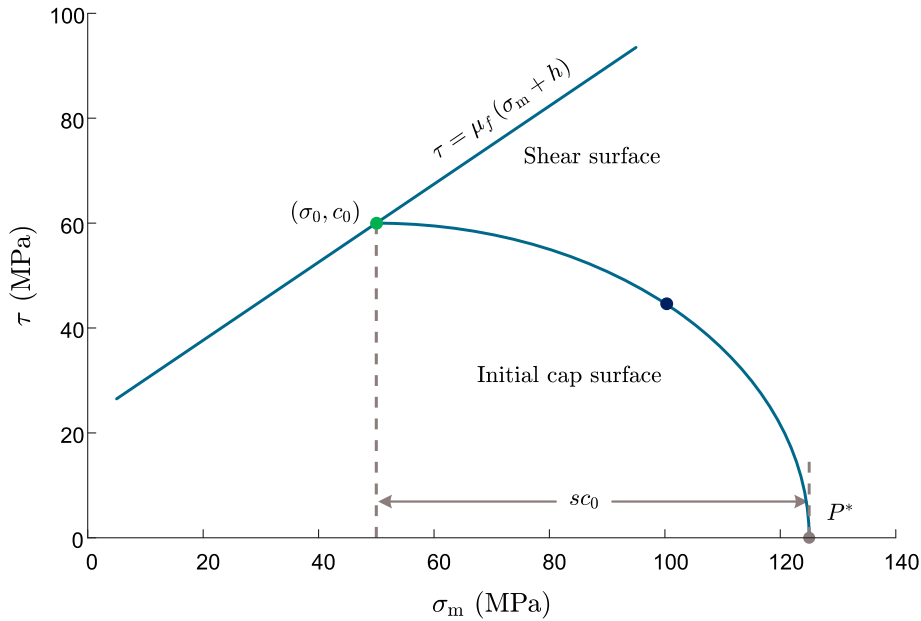


**Fig. 6** Illustration of determination method of aspect ratio $s$ from the initial cap surface

- The parameter $s'$ involved in the plastic potential can be identified by plotting the plastic volumetric strain increment at a given stress state during a high confining pressure triaxial compression test.

### 4.2 Computational aspects

The numerical computation by using the proposed elastoplastic model is based on the classic step by step iterative method, which is composed of elastic prediction and plastic correction. Once the elastic prediction is computed, one can determine the active plastic regime. The general algorithm flowchart for the $i$-th loading step can be summarized as follows:

(1) At the end of $(i-1)$ th step, the following quantities are known: $\boldsymbol{\sigma}^{(i-1)}$, $\boldsymbol{\varepsilon}^{(i-1)}$, $\boldsymbol{\varepsilon}^{\mathrm{e}(i-1)}$, $\boldsymbol{\varepsilon}^{\mathrm{ps}(i-1)}$, $\boldsymbol{\varepsilon}^{\mathrm{pc}(i-1)}$, $\gamma^{\mathrm{ps}(i-1)}$, $\varepsilon_{\mathrm{v}}^{\mathrm{pc}(i-1)}$.

(2) Given an increment of total strain $\mathrm{d}\boldsymbol{\varepsilon}^{(i)}$ and then $\boldsymbol{\varepsilon}^{(i)} = \boldsymbol{\varepsilon}^{(i-1)} + \mathrm{d}\boldsymbol{\varepsilon}^{(i)}$.

(3) Set $j = 1$ and start the iteration loop, let $\boldsymbol{\varepsilon}^{\mathrm{p}(i,0)} = \boldsymbol{\varepsilon}^{\mathrm{p}(i-1)}$, $\gamma^{\mathrm{ps}(i,0)} = \gamma^{\mathrm{ps}(i-1)}$, $\varepsilon_{\mathrm{v}}^{\mathrm{pc}(i,0)} = \varepsilon_{\mathrm{v}}^{\mathrm{pc}(i-1)}$.
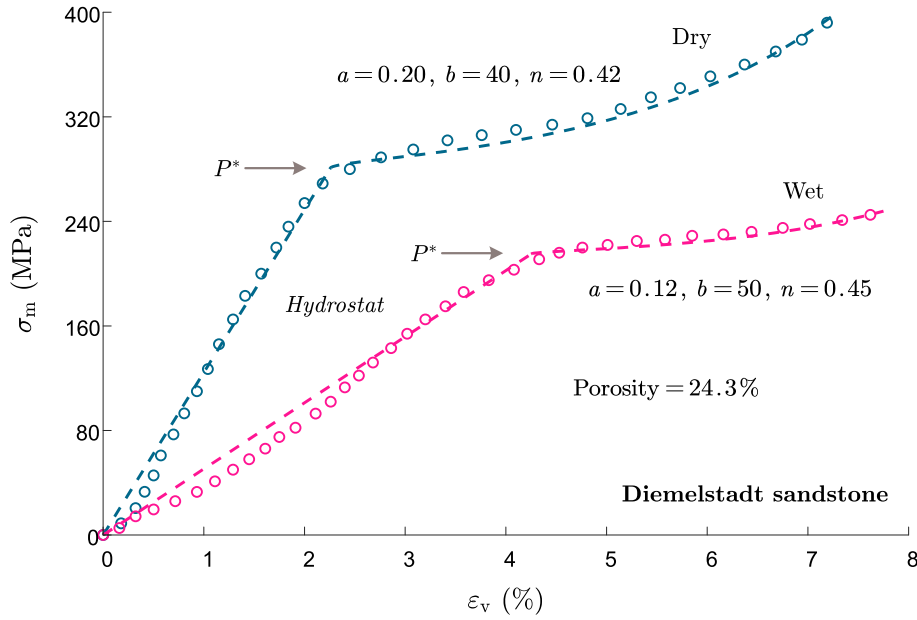
**Fig. 7** Illustration of determination method of parameters $a$, $b$ and $n$ from a hydrostatic compression test (data extracted from [61])

(4) Trial elastic prediction: $\boldsymbol{\sigma}^{(i,j)} = \mathbb{C} : \left( \boldsymbol{\varepsilon}^{(i)} - \boldsymbol{\varepsilon}^{\mathrm{p}(i,j)} \right), \gamma^{\mathrm{ps}(i,j)} = \gamma^{\mathrm{ps}(i,j-1)}, \varepsilon_{\mathrm{v}}^{\mathrm{pc}(i,j)} = \varepsilon_{\mathrm{v}}^{\mathrm{pc}(i,j-1)}$.

(5) Checking two plastic yield criteria: $f_{\mathrm{s}}^{j} \left( \boldsymbol{\sigma}^{(i,j)}, \gamma^{\mathrm{ps}(i,j)} \right)$ and $f_{\mathrm{c}}^{j} \left( \boldsymbol{\sigma}^{(i,j)}, \varepsilon_{\mathrm{v}}^{\mathrm{pc}(i,j)} \right)$.

- If $f_{\mathrm{s}}^{j} < 0$ and $f_{\mathrm{c}}^{j} < 0$, go to step (6);
- If $f_{\mathrm{s}}^{j} > 0$ and $f_{\mathrm{c}}^{j} < 0$:
  - Computation of plastic multiplier $\mathrm{d}\lambda_{\mathrm{s}}$ using Eq. (13), increment of plastic strain $\mathrm{d}\boldsymbol{\varepsilon}^{\mathrm{ps}(i,j)}$ from Eq. (11);
  - Updating of current value of plastic strain $\boldsymbol{\varepsilon}^{\mathrm{ps}(i,j)} = \boldsymbol{\varepsilon}^{\mathrm{ps}(i,j-1)} + \mathrm{d}\boldsymbol{\varepsilon}^{\mathrm{ps}(i,j)}$, shear hardening variable $\gamma^{\mathrm{ps}(i,j)} = \gamma^{\mathrm{ps}(i,j-1)} + \mathrm{d}\gamma^{\mathrm{ps}(i,j)}$ and stress $\boldsymbol{\sigma}^{(i,j)}$;
  - Updating $f_{\mathrm{s}}^{j}$, check the convergence condition: $f_{\mathrm{s}}^{j} > e$ (with $e$ being the maximum tolerance), then $j = j + 1$; else, exit from the iterative loop and go to (6).
- If $f_{\mathrm{c}}^{j} > 0$ and $f_{\mathrm{s}}^{j} < 0$:
  - Computation of plastic multiplier $\mathrm{d}\lambda_{\mathrm{c}}$ using Eq. (19), increment of plastic strain $\mathrm{d}\boldsymbol{\varepsilon}^{\mathrm{pc}(i,j)}$ from Eq. (17);
  - Updating of current value of plastic strain $\boldsymbol{\varepsilon}^{\mathrm{pc}(i,j)} = \boldsymbol{\varepsilon}^{\mathrm{pc}(i,j-1)} + \mathrm{d}\boldsymbol{\varepsilon}^{\mathrm{pc}(i,j)}$, pore collapse hardening variable $\varepsilon_{\mathrm{v}}^{\mathrm{pc}(i,j)} = \varepsilon_{\mathrm{v}}^{\mathrm{pc}(i,j-1)} + \mathrm{d}\varepsilon_{\mathrm{v}}^{\mathrm{pc}(i,j)}$, and stress $\boldsymbol{\sigma}^{(i,j)}$;
  - Updating $f_{\mathrm{c}}^{j}$, check the convergence condition: $f_{\mathrm{c}}^{j} > e$ (with $e$ being the maximum tolerance), then $j = j + 1$; else, exit from the iterative loop and go to (6).
- If $f_{\mathrm{s}}^{j} > 0$ and $f_{\mathrm{c}}^{j} > 0$:
  - Computation of two plastic multipliers $\mathrm{d}\lambda_{\mathrm{s}}$, $\mathrm{d}\lambda_{\mathrm{c}}$ using Eqs.(22) and (23), increments of plastic strains $\mathrm{d}\boldsymbol{\varepsilon}^{\mathrm{ps}(i,j)}$, $\mathrm{d}\boldsymbol{\varepsilon}^{\mathrm{pc}(i,j)}$, respectively, for two plastic mechanisms;
  - Updating of current values of plastic strains $\boldsymbol{\varepsilon}^{\mathrm{ps}(i,j)}$, $\boldsymbol{\varepsilon}^{\mathrm{pc}(i,j)}$ and plastic hardening variables $\gamma^{\mathrm{ps}(i,j)}$, $\varepsilon_{\mathrm{v}}^{\mathrm{pc}(i,j)}$, and stress $\boldsymbol{\sigma}^{(i,j)}$;
  - Updating $f_{\mathrm{s}}^{j}$ and $f_{\mathrm{c}}^{j}$, check the convergence condition: $\min \left\{ f_{\mathrm{c}}^{j}, f_{\mathrm{s}}^{j} \right\} > e$ (with $e$ being the maximum tolerance), then $j = j + 1$; else, exit from the iterative loop and go to (6).

(6) Calculate the updated values of quantities: $\boldsymbol{\sigma}^{(i)}, \boldsymbol{\varepsilon}^{(i)}, \boldsymbol{\varepsilon}^{\mathrm{ps}(i)}, \boldsymbol{\varepsilon}^{\mathrm{pc}(i)}, \gamma^{\mathrm{ps}(i)}, \varepsilon_{\mathrm{v}}^{\mathrm{pc}(i)}$.

### 4.3 Numerical simulations

The experimental data of Adamswiller sandstone and Bentheim sandstone used here are extracted from [4] and [6], respectively. By following the parameter determination procedure presented in Sect. 4.1, the values

**Table 1** Parameter values for Adamswiller sandstone and Bentheim sandstone

| | Parameters | Adamswiller | Bentheim |
|---|---|---|---|
| Elasticity | Young's modulus $E$, (MPa) | 10000 | 20000 |
| | Poisson's ratio $\nu$ | 0.20 | 0.20 |
| Plastic shearing mechanism | Initial friction coefficient $\mu_0$ | 0.20 | 0.22 |
| | Maximum friction coefficient $\mu_f$ | 0.42 | 0.48 |
| | Hydrostatic tensile strength $h$, (MPa) | 70.0 | 92.0 |
| | Plastic hardening/softening parameter $N$ | 1.40 | 1.30 |
| | Plastic equivalent shear strain at peak stress $\gamma_f^{ps}$, (%) | 0.45 | 0.55 |
| | Dilatancy coefficient $\beta_s$ | 0.30 | 0.30 |
| Plastic pore collapse mechanism | Initial plastic yield stress $\sigma_0$, (MPa) | 100.0 | 220.0 |
| | Initial plastic yield stress $c_0$, (MPa) | 72.0 | 145.0 |
| | Plastic yield function parameter $s$ | 1.54 | 1.52 |
| | Plastic hardening parameter $a$ | 2.50 | 3.50 |
| | Plastic hardening parameter $b$ | 25.0 | 15.0 |
| | Plastic hardening parameter $n$ | 0.85 | 1.02 |
| | Plastic potential function parameter $s'$ | 1.30 | 1.25 |
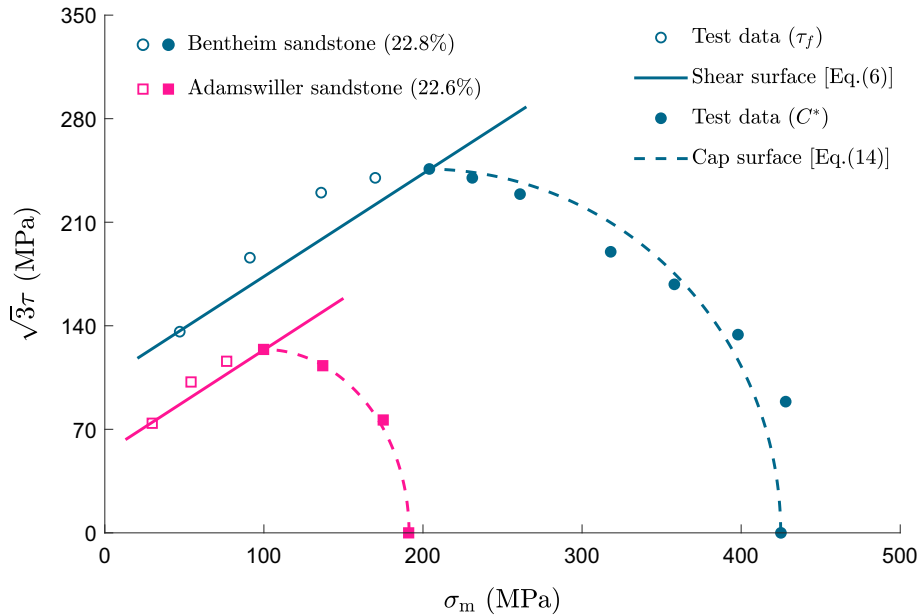


**Fig. 8** Comparisons between the two-surface model and experimental data on the peak strength ($\tau_f$) and initial yield stress ($C^*$) in conventional triaxial compression

of model's parameters for Adamswiller sandstone and Bentheim sandstone are determined and presented in Table 1.

Figure 8 shows that the two-surface model can correctly describe the mechanical behaviors of the two porous rocks for the whole range of confining pressures. More precisely, for the tests with low confining pressures, the approximate linearity of the peak strength is correctly described; for the tests with high confining pressures, the elliptical character of the initial yield stress is also correctly described.

The simulations of two hydrostatic compression tests, respectively, performed on Adamswiller sandstone and Bentheim sandstone are shown in Figs. 9 and 10. One can see that the plastic pore collapse and the plastic hardening process are well described by the model.

In Figs. 11 and 12, the deviatoric stress-volumetric strain curves of Adamswiller sandstone and Bentheim sandstone in conventional triaxial compression tests with low and high confining pressures are shown. One can see a good agreement between model's predictions and experimental data. The basic features of mechanical behaviors of the two porous rocks are reproduced, including inelastic deformation, pressure sensitivity, peak and yield strength. At low confining pressures, a brittle failure occurs with softening and dilatancy. At high confining pressures, a typical ductile failure occurs with monotonic strain hardening (shear-enhanced compaction). By
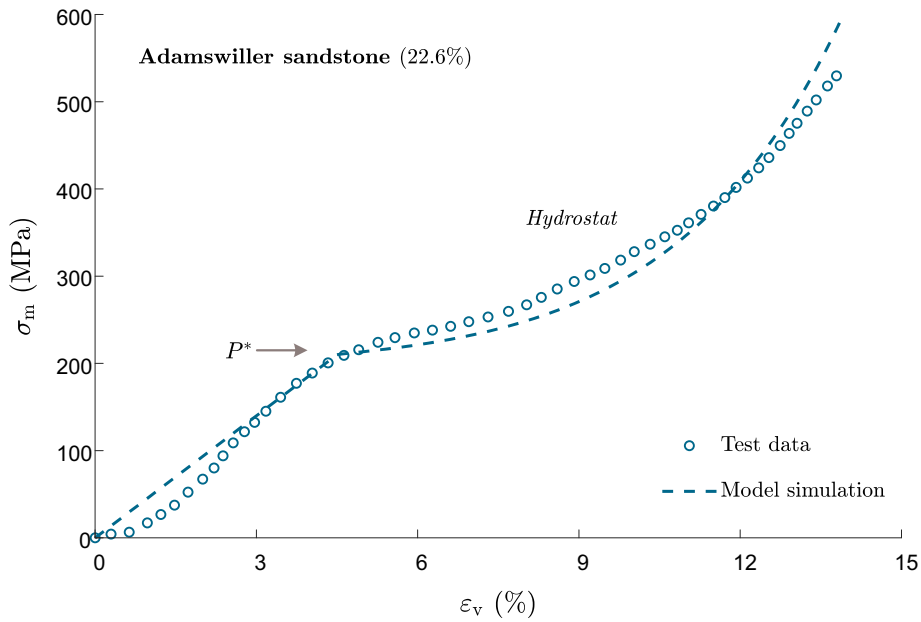
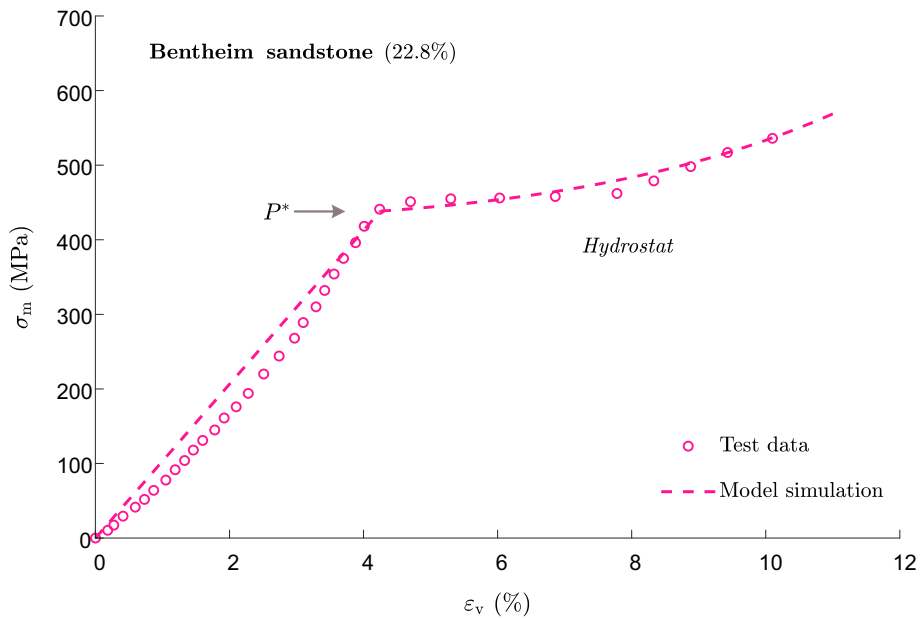**Fig. 9** Simulation of a hydrostatic compression test on Adamswiller sandstone



**Fig. 10** Simulation of a hydrostatic compression test on Bentheim sandstone

comparing the numerical simulations and experimental data, it seems that the proposed model is able to describe the brittle–ductile transition behaviors of porous rocks for the whole range of confining pressures.

Baud et al. (2006) [6] conducted detailed microstructural analysis and macroscopic observations on failed Bentheim sandstone samples, and observed that the failure mode switched from shear bands to "discrete compaction bands" at confining pressures between 120 and 350 MPa. According to Eqs. (38) and (39), the two critical confining pressures $P^{BDT}$ and $P^{CB}$ of the brittle–ductile transition for Bentheim sandstone can be, respectively, calculated as about 135 and 325 MPa. According to the prediction of localization theory, for the confining pressures ranging from 135 and 325 MPa, the failure mode should be localized in shear bands rather than "discrete compaction bands." The contradiction between theoretical prediction and experimental observation can be explained as follows. For a conventional triaxial compression test, the ratio of increment
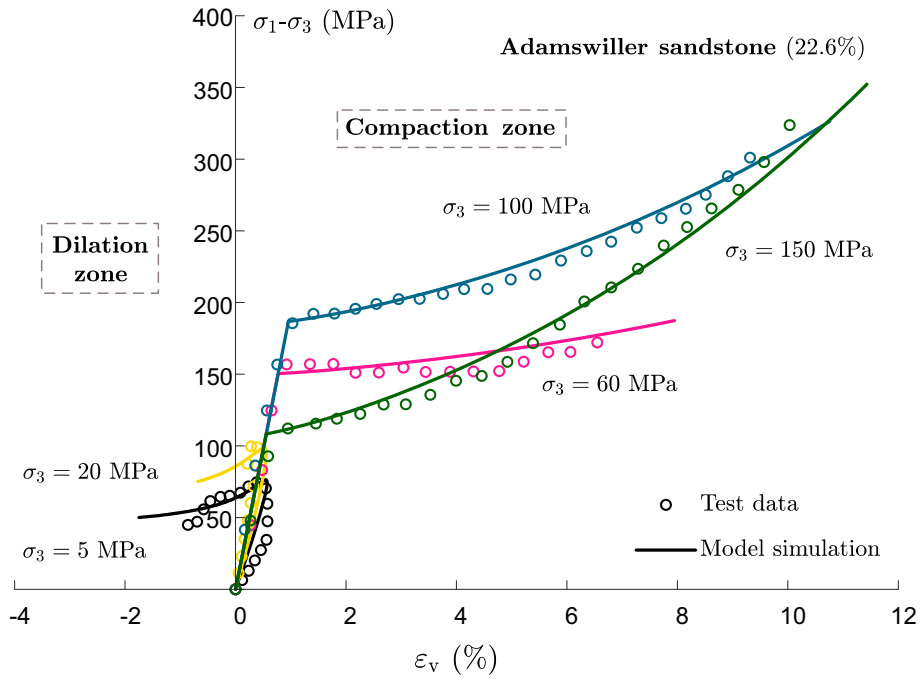
**Fig. 11** Comparisons between numerical simulation results and experimental data on Adamswiller sandstone for conventional triaxial compression tests under a wide range of confining pressures
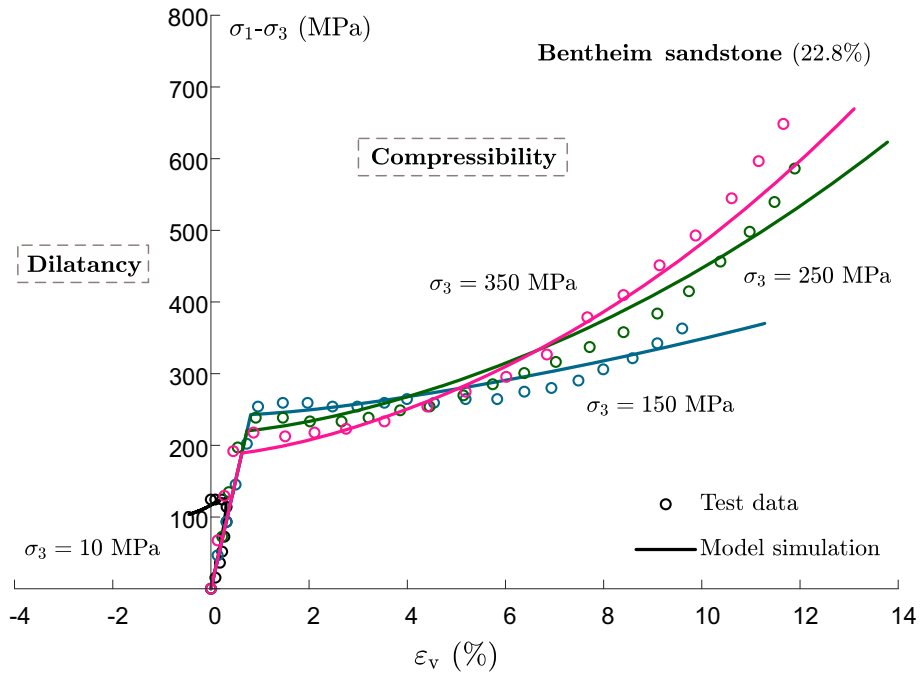


**Fig. 12** Comparisons between numerical simulation results and experimental data on Bentheim sandstone for conventional triaxial compression tests under a wide range of confining pressures

of the Mises equivalent stress to increment of the mean stress remains constant, $d\tau/d\sigma_m = \sqrt{3}$ along the non-hydrostatic stress path. The slope of the failure surface in the $(\sigma_m, \tau)$ stress space is $\mu_f = 0.48$, which is clearly lower than $\sqrt{3}$. Therefore, in the transitional regime with $\left(P^{BDT}, P^{CB}\right)$, shear localization may develop

while the sample is undergoing inelastic compaction, but this transition from compactancy to dilatancy requires significantly larger strains and higher stresses.

Unfortunately, no detailed study on the failure mode of Adamswiller sandstone are available in the literature [4]. It is then impossible to verify the model's predictive capability for the two critical confining pressures $P^{BDT}$ and $P^{CB}$ of the brittle–ductile transition for this rock.

## 5 Conclusions

In the present study, a two-surface constitutive model based on plasticity theory is proposed for the description of the brittle–ductile transition behaviors of porous rocks. Two plastic deformation mechanisms have been taken into account: plastic shearing for low confining pressures and plastic pore collapse for high confining pressures. Special functions have been proposed to describe the complexities of mechanical behaviors of porous rocks. In the case of conventional triaxial compression, an analytical solution of stress–strain relations for shear surface has been developed. When used in conjunction with bifurcation analysis, the proposed model can provide predictions of both shear and compaction localization along regions of the cap surface. Numerical simulations have been compared with experimental data for various loading conditions, including hydrostatic and triaxial compression tests, on Adamswiller sandstone and Bentheim sandstone. It has been shown that the proposed model correctly describes the main features of the mechanical behavior and brittle–ductile transition of the two porous rocks, such as inelastic deformation, peak and yield strength, volumetric compressibility–dilatancy at low confining pressures and shear-enhanced compaction at high confining pressures.

Laboratory investigations have shown that the macroscopic brittle–ductile transition of porous rocks is closely related to the microstructure. The operative deformation mechanisms under low and high confining pressures are, respectively, controlled by microcrack propagation and pore collapse. It is therefore needed in a future work to develop a micromechanics-based constitutive model to describe the brittle–ductile transition in porous rocks. And, future work will also investigate the strain localization in porous rocks based on the micromechanics-based model.

**Declarations**

**Conflict of interest** The authors declare that they have no conflict of interest.

## References

1. Paterson, M.S., Wong, T.-F.: Experimental Rock Deformation-the Brittle Field. Springer, New York, US (2005)
2. Hadizadeh, J., Rutter, E.H.: The low temperature brittle-ductile transition in a quartzite and the occurrence of cataclastic flow in nature. Geol. Rundsch. **72**(2), 493–509 (1983)
3. Rutter, E.H., Hadizadeh, J.: On the influence of porosity on the low-temperature brittle–ductile transition in siliciclastic rocks. J. Struct. Geol. **13**(5), 609–614 (1991)
4. Wong, T.-F., David, C., Zhu, W.L.: The transition from brittle faulting to cataclastic flow in porous sandstones: mechanical deformation. J. Geophys. Res. Solid Earth **102**(B2), 3009–3025 (1997)
5. Baud, P., Schubnel, A., Wong, T.-F.: Dilatancy, compaction, and failure mode in Solnhofen limestone. J. Geophys. Res. Solid Earth **105**(B8), 19289–19303 (2000)
6. Baud, P., Vajdova, V., Wong, T.-F.: Shear-enhanced compaction and strain localization: inelastic deformation and constitutive modeling of four porous sandstones. J. Geophys. Res. Solid Earth **111**(B12), 1–17 (2006)
7. Brace, W.F., Paulding, B.W., Scholz, C.H.: Dilatancy in the fracture of crystalline rocks. J. Geophys. Res. Solid Earth **71**(16), 3939–3953 (1966)
8. Zoback, M.D., Byerlee, J.D.: The effect of microcrack dilatancy on the permeability of westerly granite. J. Geophys. Res. Solid Earth **80**(5), 752–755 (1975)
9. Zhang, S.Q., Cox, S.F., Paterson, M.S.: The influence of deformation on porosity and permeability in calcite aggregates. J. Geophys. Res. Solid Earth **99**(B8), 15761–15775 (1994)
10. Moore, D.E., Lockner, D.A.: The role of microcracking in shear-fracture propagation in granite. J. Struct. Geol. **17**(1), 95–111 (1995)
11. Zhang, J.X., Wong, T.-F., Davis, D.M.: Micromechanics of pressure-induced grain crushing in porous rock. J. Geophys. Res. Solid Earth **95**(B1), 341–352 (1990)
12. Hirth, G., Tullis, J.: The brittle-plastic transition in experimentally deformed quartz aggregates. J. Geophys. Res. Solid Earth **99**(B6), 11731–11747 (1994)

13. Menéndez, B., Zhu, W.L., Wong, T.-F.: Micromechanics of brittle faulting and cataclastic flow in berea sandstone. J. Struct. Geol. **18**(1), 1–16 (1996)

14. Zhu, W.L., Wong, T.-F.: The transition from brittle faulting to cataclastic flow: permeability evolution. J. Geophys. Res. Solid Earth **102**(B2), 3027–3041 (1997)

15. Zhu, W., Baud, P., Wong, T.-F.: Micromechanics of cataclastic pore collapse in limestone. J. Geophys. Res. Solid Earth **115**(B4), 1–17 (2010)

16. Shao, J.F., Jia, Y., Kondo, D., Chiarelli, A.S.: A coupled elastoplastic damage model for semi-brittle materials and extension to unsaturated conditions. Mech. Mater. **38**(3), 218–232 (2006)

17. Chen, D., Shen, W.Q., Shao, J.F., Yurtdas, I.: Micromechanical modeling of mortar as a matrix-inclusion composite with drying effects. Int. J. Numer. Anal. Methods Geomech. **37**(9), 1034–1047 (2013)

18. Nguyen, L.D., Fatahi, B., Khabbaz, H.: A constitutive model for cemented clays capturing cementation degradation. Int. J. Plast **56**, 1–18 (2014)

19. Desai, C.S., Siriwardane, H.J.: Constitutive Laws for Engineering Materials with Emphasis on Geologic Materials. Prentice-Hall, New Jersey (1984)

20. A. F. Fossum and J. T. Fredrich: Cap plasticity models and compactive and dilatant pre-failure deformation, in *Proc. 4th North American Rock Mechanics Symposium, A. A. Balkema, Rotterdam*, 2000, pp. 1169–1176

21. Grueschow, E., Rudnicki, J.W.: Elliptic yield cap constitutive modeling for high porosity sandstone. Int. J. Solids Struct. **42**(16), 4574–4587 (2005)

22. Schofield, A., Wroth, P.: Critical State Soil Mechanics. McGraw-Hill, New York, US (1968)

23. Dimaggio, F.L., Sandler, I.S.: Material model for granular soils. J. Eng. Mech. **97**(3), 935–950 (1971)

24. Wood, D.M.: Soil Behaviour and Critical State Soil Mechanics. Cambridge University Press, Cambridge (1990)

25. Cuss, R.J., Rutter, E.H., Holloway, R.F.: The application of critical state soil mechanics to the mechanical behaviour of porous sandstones. Int. J. Rock Mech. Min. Sci. **40**(6), 847–862 (2003)

26. Schultz, R.A., Siddharthan, R.: A general framework for the occurrence and faulting of deformation bands in porous granular rocks. Tectonophysics **411**(1), 1–18 (2005)

27. Foster, C.D., Regueiro, R.A., Fossum, A.F., Borja, R.I.: Implicit numerical integration of a three-invariant, isotropic/kinematic hardening cap plasticity model for geomaterials. Comput. Methods Appl. Mech. Eng. **194**, 5109–5138 (2005)

28. Tamagnini, C., Ciantia, M.O.: Plasticity with generalized hardening: constitutive modeling and computational aspects. Acta Geotech. **11**(3), 595–623 (2016)

29. Bennett, K.C., Borja, R.I.: Hyper-elastoplastic/damage modeling of rock with application to porous limestone. Int. J. Solids Struct. **143**(3), 218–231 (2018)

30. Lv, Z.T., Luo, S.C., Xia, C.C., Zeng, X.T.: A thermal-mechanical coupling elastoplastic model of Freeze-Thaw deformation for porous rocks. Rock Mech. Rock Eng. **55**(6), 3195–3212 (2022)

31. Fossum, A.F., Senseny, P.E., Pfeifle, T.W., Mellegard, K.D.: Experimental determination of probability distributions for parameters of a Salem limestone cap plasticity model. Mech. Mater. **21**(2), 119–137 (1995)

32. Olsson, W.A.: Theoretical and experimental investigation of compaction bands in porous rock. J. Geophys. Res. Solid Earth **104**(B4), 7219–7228 (1999)

33. Fossum, A.F., Fredrich, J.T.: Constitutive Models for the Etchegoin Sands, Belridge Diatomite, and Overburden Formations at the Lost Hills Oil Field, California, Technical Report SAND2000-0827. Sandia National Laboratories. Albuquerque, US (2000)

34. Desai, C.S.: A general basis for yield, failure and potential functions in plasticity. Int. J. Numer. Anal. Methods Geomech. **4**(4), 361–375 (1980)

35. Shao, J.F., Henry, J.P.: Validation of an elastoplastic model for chalk. Comput. Geotech. **9**(4), 257–272 (1990)

36. Shao, J.F., Henry, J.P.: Development of an elastoplastic model for porous rock. Int. J. Plast **7**(1), 1–13 (1991)

37. Homand, S., Shao, J.F.: Mechanical behaviour of a porous chalk and water/chalk interaction. Oil Gas Sci. Technol. **55**(6), 591–598 (2000)

38. Lin, J., Xie, S.Y., Shao, J.F., Kondo, D.: A micromechanical modeling of ductile behavior of a porous chalk: formulation, identification, and validation. Int. J. Numer. Anal. Methods Geomech. **36**(10), 1245–1263 (2012)

39. Xie, S.Y., Shao, J.F.: Experimental investigation and poroplastic modelling of saturated porous geomaterials. Int. J. Plast **39**, 27–45 (2012)

40. Jia, Y., Zhao, X.L., Bian, H.B., Wang, W., Shao, J.F.: Numerical modelling the influence of water content on the mechanical behaviour of concrete under high confining pressures. Mech. Res. Commun. **119**(6), 103819 (2022)

41. Lade, P.V., Kim, M.K.: Single hardening constitutive model for soil, rock and concrete. Int. J. Solids Struct. **32**(14), 1963–1978 (1995)

42. Ehlers, W.: A single-surface yield function for geomaterials. Arch. Appl. Mech. **65**(4), 246–259 (1995)

43. Khoei, A.R., Azami, A.R.: A single cone-cap plasticity with an isotropic hardening rule for powder materials. Int. J. Mech. Sci. **47**(1), 94–109 (2005)

44. Zhao, L.-Y., Shao, J.-F., Zhu, Q.-Z.: Analysis of localized cracking in quasi-brittle materials with a micro-mechanics based friction-damage approach. J. Mech. Phys. Solids **119**, 163–187 (2018)

45. Baud, P., Klein, E., Wong, T.-F.: Compaction localization in porous sandstones: spatial evolution of damage and acoustic emission activity. J. Struct. Geol. **26**(4), 603–624 (2004)

46. Vajdova, V., Zhu, W., Chen, T.M.N., Wong, T.-F.: Micromechanics of brittle faulting and cataclastic flow in tavel limestone. J. Struct. Geol. **32**(8), 1158–1169 (2010)

47. Wong, T.-F., Baud, P.: The brittle–ductile transition in porous rock: a review. J. Struct. Geol. **44**, 25–53 (2012)

48. Zhu, Q.Z.: Strength prediction of dry and saturated brittle rocks by unilateral damage-friction coupling analyses. Comput. Geotech. **73**, 16–23 (2016)

49. Zhao, L.Y., Zhu, Q.Z., Shao, J.F.: A micro-mechanics based plastic damage model for quasi–brittle materials under a large range of compressive stress. Int. J. Plast **100**, 156–176 (2018)

50. Zhao, L.Y., Zhang, W.L., Lai, Y.M., Niu, F.J., Zhu, Q.Z., Shao, J.F.: A heuristic elastoplastic damage constitutive modeling method for geomaterials: from strength criterion to analytical full-spectrum stress-strain curves. Int. J. Geomech. **21**(2), 04020255 (2021)
51. Brace, W.F.: Volume changes during fracture and frictional sliding: A review. Pure Appl. Geophys. **116**(4), 603–614 (1978)
52. Vajdova, V., Baud, P., Wong, T.-F.: Compaction, dilatancy, and failure in porous carbonate rocks. J. Geophys. Res. Solid Earth **109**(B5), 1–16 (2004)
53. Wong, T.-F., Szeto, H., Zhang, J.: Effect of loading path and porosity on the failure mode of porous rocks. Appl. Mech. Rev. **45**(8), 281–293 (1992)
54. Zhu, W., Baud, P., Vinciguerra, S., Wong, T.-F.: Micromechanics of brittle faulting and cataclastic flow in Alban hills tuff. J. Geophys. Res. Solid Earth **116**(B6), 1–23 (2011)
55. Shen, W.Q., Shao, J.F.: An elastic–plastic model for porous rocks with two populations of voids. Comput. Geotech. **76**, 194–200 (2016)
56. Han, B., Shen, W.Q., Xie, S.Y., Shao, J.F.: Plastic modeling of porous rocks in drained and undrained conditions. Comput. Geotech. **117**, 103277 (2020)
57. Zhao, L.Y., Lai, Y.M., Shao, J.F.: A new incremental variational micro-mechanical model for porous rocks with a pressure-dependent and compression-tension asymmetric plastic solid matrix. Int. J. Rock Mech. Min. Sci. **153**, 105059 (2022)
58. Rudnicki, J.W., Rice, J.R.: Conditions for the localization of deformation in pressure-sensitive dilatant materials. J. Mech. Phys. Solids **23**(6), 371–394 (1975)
59. Issen, K.A., Rudnicki, J.W.: Conditions for compaction bands in porous rock. J. Geophys. Res. Solid Earth **105**(B9), 21529–21536 (2000)
60. Issen, K.A., Rudnicki, J.W.: Theory of compaction bands in porous rock. Phys. Chem. Earth Pt A **26**(1–2), 95–100 (2001)
61. Tembe, S., Baud, P., Wong, T.-F.: Stress conditions for the propagation of discrete compaction bands in porous sandstone. J. Geophys. Res. Solid Earth **113**(B9), 1–16 (2008)